Impact of ink synthesis on processing of inkjet-printed silicon nanoparticle thin films: A comparison of Rapid Thermal Annealing and photonic sintering

Etienne Drahi, Sylvain Blayac, Andras Borbely, Patrick Benaben

▶ To cite this version:

Etienne Drahi, Sylvain Blayac, Andras Borbely, Patrick Benaben. Impact of ink synthesis on processing of inkjet-printed silicon nanoparticle thin films: A comparison of Rapid Thermal Annealing and photonic sintering. Thin Solid Films, 2015, 574, pp.169-176. 10.1016/j.tsf.2014.11.079 . emse-01500467

HAL Id: emse-01500467
https://hal-emse.ccsd.cnrs.fr/emse-01500467

Submitted on 23 Apr 2024

HAL is a multi-disciplinary open access archive for the deposit and dissemination of scientific research documents, whether they are published or not. The documents may come from teaching and research institutions in France or abroad, or from public or private research centers.

L'archive ouverte pluridisciplinaire **HAL**, est destinée au dépôt et à la diffusion de documents scientifiques de niveau recherche, publiés ou non, émanant des établissements d'enseignement et de recherche français ou étrangers, des laboratoires publics ou privés.

Impact of ink synthesis on processing of inkjet-printed silicon nanoparticle thin films: A comparison of Rapid Thermal Annealing and photonic sintering

E. Drahi [a], S. Blayac [a], A. Borbely [b], P. Benaben [a]

[a]Centre Microélectronique de Provence/Ecole Nationale Supérieure des Mines de Saint Etienne, 880, avenue de Mimet Gardanne, 13541, France
[b]Science des Matériaux et des Structures/Ecole Nationale Supérieure des Mines de Saint Etienne, 158, cours Fauriel Saint Etienne Cedex 2, 42023, France

Inkjet printing has a high potential for cost reduction in solar cell and thermoelectric industry. This study demonstrates that silicon thin films can be produced by inkjet-printing of silicon nanoparticles followed by sub-sequent drying and annealing steps. Ink formulation is crucial for the sintering of the silicon nanoparticles and control of the microstructure at low temperature. Upon heating, the microstructure is modified from porous layer made of juxtaposed silicon nanoparticles to denser layer with coarser grains. This evolution is monitored by scanning electron microscopy and by micro-Raman spectroscopy, which offer a fast and precise characteriza-tion of the microstructure and chemical composition of thin films. Above a threshold temperature of 800 °C cracks appear within thin film and substrate because of the stress induced by the oxidation of the surface. An in-novative sintering method, photonic annealing, is studied in order to reduce both oxidation and stress in the thin films as well as reducing processing time. Evolution of the thermal conductivity is performed by micro-Raman spectroscopy and can be tailored in a large range between ~1 and ~100 $W \cdot m^{-1} \cdot K^{-1}$ depending on the sintering method and atmosphere. Therefore control of the microstructure evolution with applied annealing process allows tailoring of both microstructure and thermal conductivity of the silicon thin films.

1. Introduction

Inkjet-printing has been seen as a very promising way to deposit and pattern a broad choice of materials on large areas for low costs. Nowadays, ink based on metallic nanoparticles and polymers are widely used for flexible electronics [1–4]. Nevertheless, organic semiconductor efficiency and lifetime are clearly behind those of inorganic semiconductors, which limit strongly the field of applications for printed electronics. Therefore, solution-processing of inorganic semiconductors appears as a promising way to fabricate high-performance devices at low costs [5].

Silicon is the most employed semiconductor for electronic applications due to its availability, its useful oxide, its performances and good process know-how developed throughout the years in microelectronics. Deposition of silicon by solution-processing is therefore researched in order to lower fabrication costs without developing new materials and device architectures [6–9]. Furthermore, very specific properties (band gap broadening, photoluminescence…) appear by reducing silicon into nanosized-objects (nanoparticles, nanorods, nanowires…), as well as the possibility to use solution-based processes such as inkjet-printing. Therefore, the control of inkjet-printing of silicon nanoparticles (NPs) opens a way towards the fabrication of low cost electronic devices with tailored properties.

After inkjet-printing deposition and drying of the Si nanoparticle-based inks, thin films ranging from some hundreds of nanometers to some micrometers can be obtained. They are composed of juxtaposed nanoparticles in punctual contact and as a result are very porous. Electrical conductivity of such thin films is very limited [8,10] since the percolation threshold has to be reached [11], especially if the particles are not doped.

An annealing step is therefore needed in order to modify the microstructure (densification or grain coarsening) by sintering [12] to permit charge carrier transport [13]. For example, conductivities ranging between 10^{-8} and 5 $\Omega^{-1} \cdot cm^{-1}$ could be obtained after laser annealing depending on both laser pulse energy and doping level of the silicon nanoparticles [14]. Those values guaranty sufficient carrier transport for thermoelectrics and photovoltaics devices' performance. This paper studies the evolution of the microstructure upon annealing depending on the nanoparticle surface chemistry due to the ink synthesis as well as the impact of the sintering atmosphere and method. Photonic annealing – especially developed for printed electronics – is compared to more classic annealing methods (Rapid Thermal Annealing).

2. Experimental details

2.1. Materials

Two commercial silicon nanoparticle-based suspensions (inks) were developed for our purposes and purchased from Meliorum Technologies Incorporation (Product #09820). Nonetheless, the supplier kept the synthesis procedure confidential. The undoped nanoparticles obtained from chemical synthesis, the same for both inks, have a diameter ranging between 20 nm and 150 nm (Fig. 1). They were put in suspension in ethylene glycol (reagent grade) with a concentration of ~1 wt.%. Concerning one of the two inks, some trace of water has been identified. This issue will be discussed in the following.

Following inks were studied: ink 1 with addition of 0.1 μM of sodium dodecylbenzenesulfonate and ink 2 with addition of sodium polymethacrylate (NaPMA) in an uncontrolled concentration (Na content of 144 mg/L was measured afterwards by atomic absorption). These components are commonly added in order to improve the stability of the suspension and to protect the nanoparticles against oxidation.

Viscosities (measured with a Brookfield DV1 + dynamic viscosimeter, rotating spindle) and surface tensions (measured through the pendant drop method with OCA 200 goniometer from Apollo Instruments) at room temperature are respectively of 24 mPa·s and 39 mN/m for ink 1 and of 13 mPa·s and 46 mN/m for ink 2.

2.2. Inkjet-printing process

A drop on demand system (Dimatix printer DMP 2800) was used for printing of Si nanoparticle inks using specifically designed waveforms. Silica glass substrates (reference JGS1 purchased from ACM) with average roughness $R_a = 0.62$ nm (measured with a Veeco Atomic Force Microscope SP-II) were used. An initial cleaning was performed with acetone in ultrasonic bath before printing. Surface energy of 47 ± 1 mN/m was calculated from goniometric measurements with three different liquids (water, ethylene glycol & diiodomethane) using the Owens–Wendt–Rabel–Kälble model [15].

Drop spacing of 20 μm between two consecutive drop centers was identified as being optimal. In order to increase the layer thickness two passes printing was applied without intermediate drying or annealing.

The printing step was followed by a two-steps drying process: 1) at room temperature under vacuum (<1 mbar) and 2) drying at 200 °C under nitrogen for 5 min in order to evaporate the ethylene glycol. It resulted in the layer morphology described in Fig. 2 Layers (11×11 mm^2) exhibit a squared coffee ring [16] structure with a flat part (~1 μm thick) at the center.

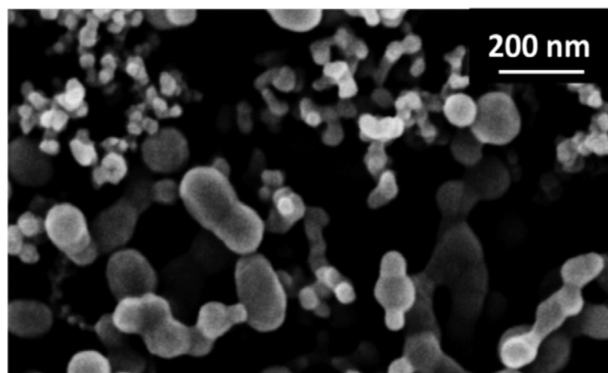

Fig. 1. Scanning Electron Microscope picture of Si nanoparticles after evaporation of the ink solvents at 200 °C.

a) After printing

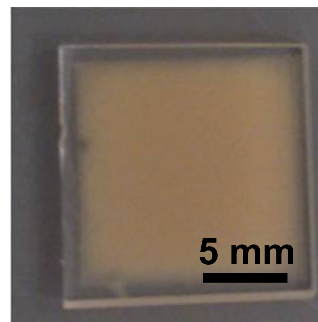

b) Vacuum drying

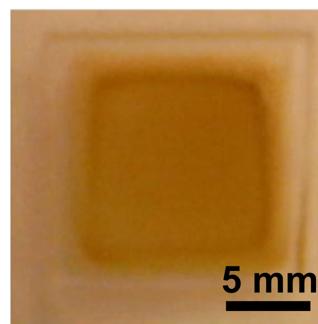

c) Cross-section representation of the printed

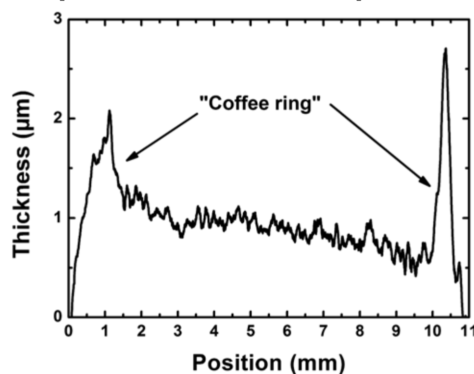

Fig. 2. a, b) Pictures and schematic cross-section representations of a printed layer just before and after vacuum drying at room temperature. c) Cross-section obtained by mechanical profilometry of a Rapid Thermal Annealing (RTA) of the layer at 700 °C for better mechanical behavior.

2.3. Annealing processes

Two types of annealing processes were studied for functional properties recovering of the thin films: Rapid Thermal Annealing (RTA) and photonic annealing.

Concerning RTA, a Jipelec jetfirst furnace equipped with 12 halogen lamps of 144 V–1200 W was used. Temperatures ranging from 600 °C to 1000 °C were applied (dwell times of 5 min and heating rate of 50 °C/s) under two types of atmosphere: inert atmosphere N_2 (99.999% purity) and reducing atmosphere N_2 (H_2 — 5%, 99.999% purity).

Photonic annealing was performed on a PulseForge system (PF3200-X1 from NovaCentrix) equipped with two broad spectrum high-intensity discharge lamps (XP-447 from NovaCentrix). The discharge

lamps are filled with high pressure of xenon gas that arcs with high current and produces a spectrum of light that encompasses ultraviolet to infrared (210 to 1800 nm). The lamps are designed to turn on and off on microsecond time scale, emitting a high intensity of light in the process.

In this work, short pulse lengths (μs to ms) are used to heat the surface layer faster than the quenching into the substrate; resulting in selective sintering on the surface. Fig. 3 represents the different types of pulses shapes: monopulse cycle and micropulses (μpulses) cycle; resulting in different delivered powers [17]. Delivered power is controlled through the capacitor voltages and was set at 380 V for ideal performance. The resulting pulse conditions produced theoretical power densities from 6.75–10 kW/cm^2 and radiant exposures from 4–6 J/cm^2.

Table 1 summarizes the different processes applied to the samples. The pulse parameters as well as the theoretical estimated energy and power calculated from the amplitude and pulse length, are also indicated. A previous study, comparing the theoretical equivalent energy obtained from the area under the waveform and the energy measured with a bolometer inside the equipment, demonstrated a maximal discrepancy between both values inferior to 1 J/cm^2.

For monopulse cycles the long pulse length provokes variation of the delivered power over time. For example, for process no. 3 (Table 1), which is the longer monopulse cycle, delivered power varies between ~10 kW/cm^2 and 7 kW/cm^2. By using micropulse cycles the delivered power can be kept closer to the maximal value over time; resulting in higher temperature elevation of the sample (see Results & discussions section) (Fig. 3).

For photonic annealing, after drying, samples were placed into a chamber filled with inert gas in order to minimize oxidation of the sample upon annealing. Each process (described in Table 1) was repeated 1, 2 and 5 times.

2.4. Characterization of suspensions

Both inks were analyzed by Fourier Transform Infrared Spectroscopy (FTIR) using a Bruker Vertex 70 spectrometer with an attenuated total reflectance system. Simultaneous thermogravimetric analysis (TGA) and differential scanning calorimetry (DSC) — TA instrument SDT Q600, were also applied (10 °C/min heating rate in N_2 atmosphere, 99.999% purity).

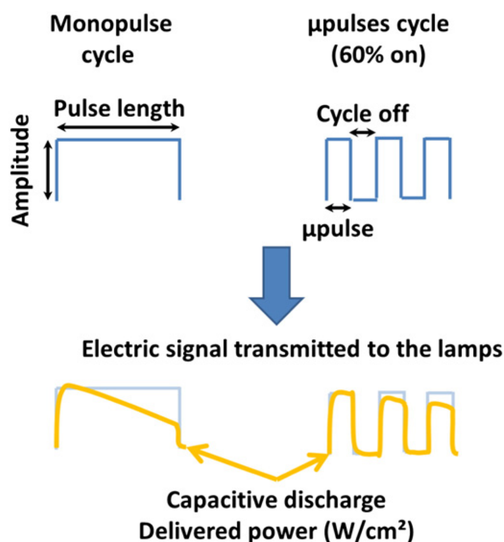

Fig. 3. Different photonic annealing pulses and their impact on the capacitive discharge (delivered power) transmitted to the lamps.

Table 1
Parameters for the photonic annealing processes.

Process no.	1	2	3	4	5
Amplitude (V)	380	380	380	380	380
Pulse length (μs)	500	600	690	1300	1300
Quantity of μpulses	–	–	–	3	4
Duty cycle (on/off)	1	1	1	0.5	0.6
Length of μpulses (μs)	–	–	–	217	195
Theoretical equivalent energy (J/cm^2)	4.3	5.5	5.68	4.91	5.56
Theoretical developed power (kW/cm^2)	10–8	10–7.5	10–7	10–7.5	10–6.75

2.5. Characterization of the sintered thin films

Properties of sintered Si NP thin films were characterized first using the following equipments: Carl Zeiss Ultra 55 SEM (3 kV tube voltage, corresponding filament intensity 2.360 A and extraction intensity 242.60 μA) and micro-Raman spectroscopy — Jobin-Yvon LabRam 800 HR equipped with two laser wavelengths (488 nm and 633 nm).

Evaluation of mechanical stress σ close to the surface was obtained by Raman spectroscopy using the Raman shift method [6,18]. These values were compared to the ones obtained by Grazing Incidence–X-Ray Diffraction (GI–XRD) measurements performed using $sin^2\psi$ method [19] with Panalytical X'Pert MRD diffractometer equipped with a sealed Co tube and operated at 45 kV and 40 mA. The stress was evaluated from the displacements of the 311 peak of the Si (2θ ~ 66.29°) as a function of $sin^2\psi$.

Raman spectroscopy was also used to measure the thermal conductivity of the thin films. Local temperature elevation can be measured through the Raman shift method [18]. This temperature is thereafter introduced into Eq. 1, which is an approximation of Nonnenmacher work [20] for thin films [8]:

$$\kappa = \frac{\left(d - {}^{1}\!/_{2\alpha}\right) P_{abs}}{\Delta T} \quad (1)$$

where d is the layer thickness, α the absorption coefficient of the material, P_{abs} the absorbed power of the laser by the material and ΔT the temperature gradient on the film. 1 μm thick layers were measured by mechanical profilometry. The optical parameters ($\alpha = 5.10^4$ cm^{-1} and reflection of 30%) have been estimated from [8] for the probed wavelengths.

3. Results and discussions

3.1. Si nanoparticle surface chemistry impact on drying process, sintering and melting

DSC/TGA and FTIR measurements on both inks have been led in order to optimize the drying and annealing processes as well as observing the impact of the nanoparticle surface chemistry.

Concerning FTIR (Fig. 4), the biggest difference is in the 1500 cm^{-1}–1800 cm^{-1} region where $\nu(C=O)$ and $\nu(COO)$ mode peaks attributed to NaPMA are observed for ink 2. It shows lower oxidation than ink 1 as the reduced intensity of $\nu(Si–O–Si)$ mode peaks and the presence of a small $\nu(Si–H)$ mode peak show. It is therefore suspected that the introduction of NaPMA protects at some extent a surface of Si nanoparticles against oxidation. Furthermore $\delta(Si–CH_2)$ bands have been observed and could be attributed to bond formation between Si nanoparticle surface and ethylene glycol or other reagent used during the nanoparticle chemical synthesis developed by the supplier.

DSC/TGA measurements (Fig. 5) demonstrate for both inks an endothermic peak located around 170 °C attributed to the evaporation of ethylene glycol.

Concerning ink 2 (NaPMA functionalized nanoparticles) another peak attributed to water evaporation is located around 90 °C. It is

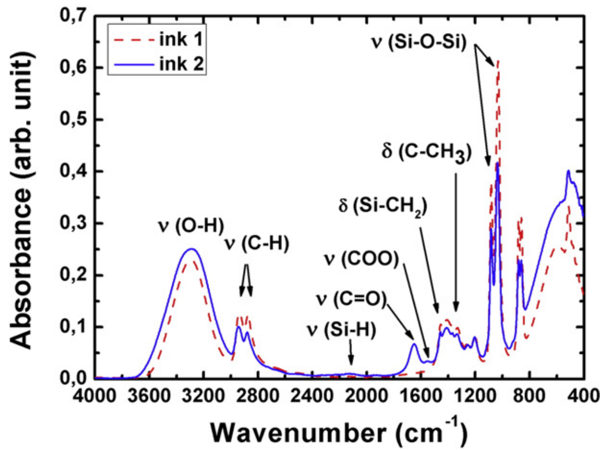

Fig. 4. FTIR analysis of both silicon inks.

supposed that NaPMA acts like sodium polyacrylate (NaPA) absorbing water very easily [21]. Reduced boiling temperature, around 10% lower than what can be found in literature, is attributed to the small quantity of solvents involved in the measurement.

A room temperature drying step was thus added in order to control evaporation of water traces that were found in ink 2 and avoid ink migration and heterogeneous thickness of dried layers.

Concerning ink 2, the endothermic peak at 800 °C is attributed to the melting of the tiniest Si nanoparticles (~20 nm). Indeed, different models predict a decrease of the melting temperature with size reduction for spherical nanoparticles [22–25]. Experimental data show good global agreement with the theoretical models [26–28].

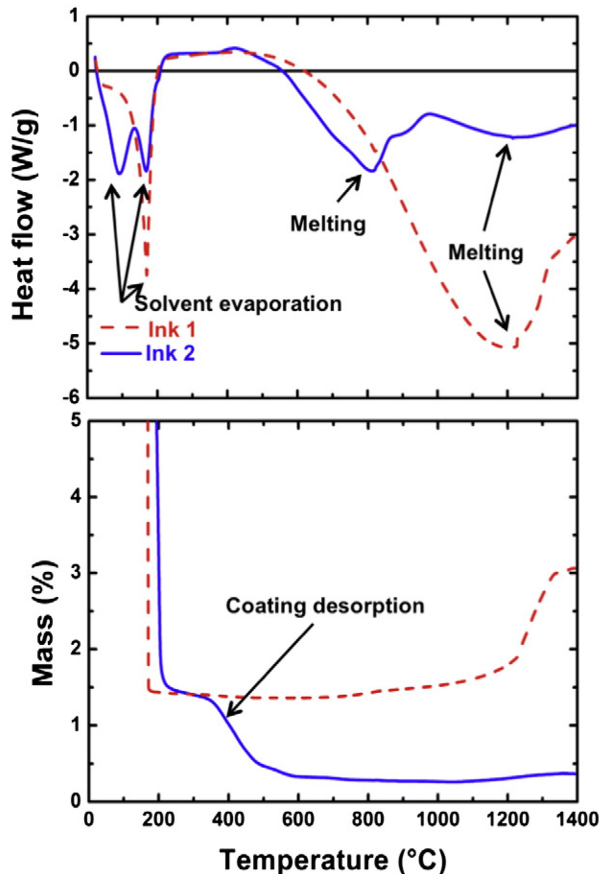

Fig. 5. DSC/TGA measurement of both inks. Exothermic and endothermic heat flows are directed upward and downward respectively.

Concerning ink 1, melting of the tiniest nanoparticles (~20 nm) happens only around 1200 °C as demonstrated by the endothermic peak. Higher temperature in comparison with ink 2 is due to higher oxidation state of the nanoparticles as FTIR experiments demonstrated. Therefore, the melting is only possible for temperatures above 1100 °C where reduction of silicon dioxide by silicon is possible [10,29,30].

$$SiO_{2(s)} + Si_{(s)} \leftrightarrow 2SiO_{(g)} \quad (2)$$

Surface chemistry control of Si nanoparticles is decisive in order to reduce the temperature of annealing processes. Ink 2 (with NaPMA) was chosen with this objective. All the following results were obtained using it due to its lower melting temperature. It is supposed that the NaPMA coating reduced strongly the oxidation state of the Si nanoparticles provoking an incomplete oxide shell around the nanoparticles when protecting organics are removed in an inert and pure atmosphere. It therefore allows heat conduction into the nanoparticle core as well as sintering and melting at a lower temperature.

Finally, for both inks a mass increase is observed above 1200 °C (Fig. 5). It is attributed to oxidation of the silicon surface by residual oxygen. Nonetheless, mass increase is much smaller in the case of ink 2, which tends to corroborate the lower oxidation state of the material.

3.2. Rapid Thermal Annealing of inkjet-printed Si nanoparticles thin films

SEM observations show that the microstructure of the thin film can be controlled from a porous (600 °C–800 °C) to a denser material with coarser grains (>800 °C). For samples annealed at 900 and 1000 °C cracks can be observed in the layers (Fig. 6).

The calculated bi-axial stress σ values, obtained from Raman measurements, are plotted in Fig. 7. Tensile stress is attributed to the difference of thermal expansion coefficients α between the silicon thin film and the substrate during cooling. Theoretical produced stress σ_f is given by:

$$\sigma_f = \left(\frac{E_f}{1-\nu_f}\right)\left(\alpha_f - \alpha_s\right)\Delta T \quad (3)$$

where E_f, ν_f and α_f are the Young's modulus, Poisson's coefficient and expansion coefficient of the Si thin film and α_s the expansion coefficient of the substrate.

σ_f was calculated using parameters of bulk silicon ($E_f = 163$ GPa, $\nu_f = 0.23$ et $\alpha_f = 2.6.10^{-6}$ °C^{-1}) and $\alpha_s = 6.0.10^{-7}$ °C^{-1} (gray dash curve on Fig. 7). These values fit well the measured values up to annealing temperatures of 800 °C. This result was expected since Si bulk values and semi-empirical relationships have been used for stress calculation either from the Raman measurement or thermal expansion coefficient difference upon cooling.

Nevertheless, these values are much higher than the stress usually reported for nanoparticle-based thin films and measured using the $sin^2\psi$ XRD method [31,32]. The lower stresses were attributed to porosity-induced relaxation.

Micro-Raman probed volume is smaller than in GI–XRD measurements. Concerning the latter, the peak of the silica glass substrate around 22° confirms that the complete Si thin film thickness is analyzed (Fig. 8) over a surface area of mm^2 (here 14 × 15 mm^2). Concerning Raman, the measurement allows analysis of an area of only a few hundred of nm^2 to ~1 μm^2 with a probing depth d_p [18]:

$$d_p \cong {}^{2.3}\!\Big/_{2\alpha} \quad (4)$$

where α is the absorption coefficient at the wavelength of the probing laser. It results in probing depths of around 200 nm and 600 nm for laser wavelengths of 488 nm and 633 nm, respectively (α taken from [8]).

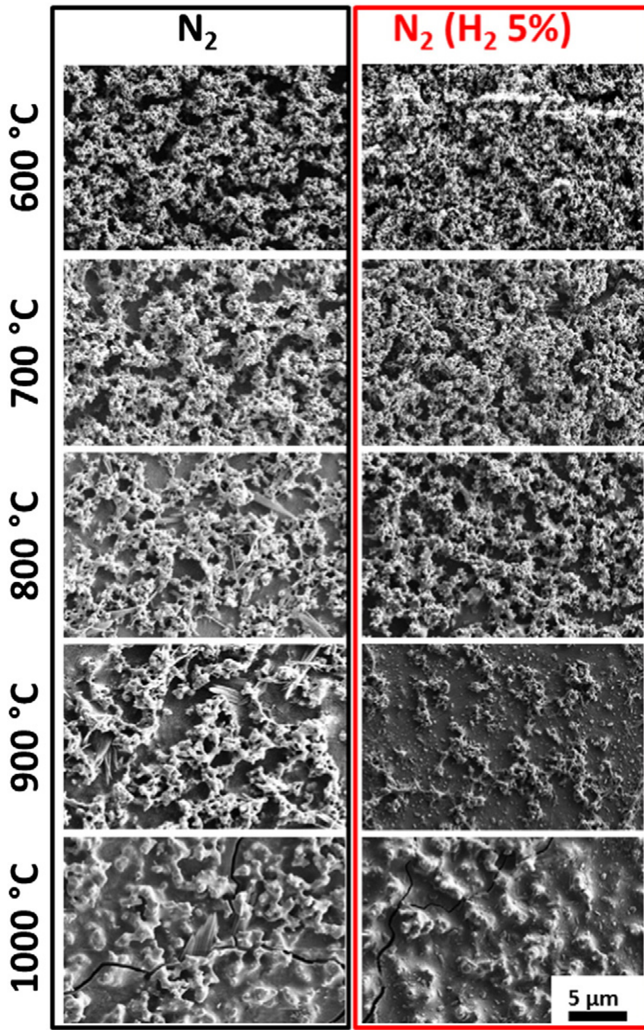

Fig. 6. SEM pictures of RTA annealed layers in both atmospheres at different temperatures.

By micro-Raman it is very likely that only a few grains (maybe only one) are probed, while GI–XRD measurements give information about tens of grains and therefore an average of stress over the microstructure.

Compressive stress is attributed to oxidation of the Si grains [33,34]. Preferred oxidation of grain boundaries compresses Si grains. GI–XRD measurements (Fig. 8) confirm creation of two silicon dioxides (JCPDS 04-007-5015 and JCPDS 01-082-1570) for annealing at temperatures superior to 800 °C.

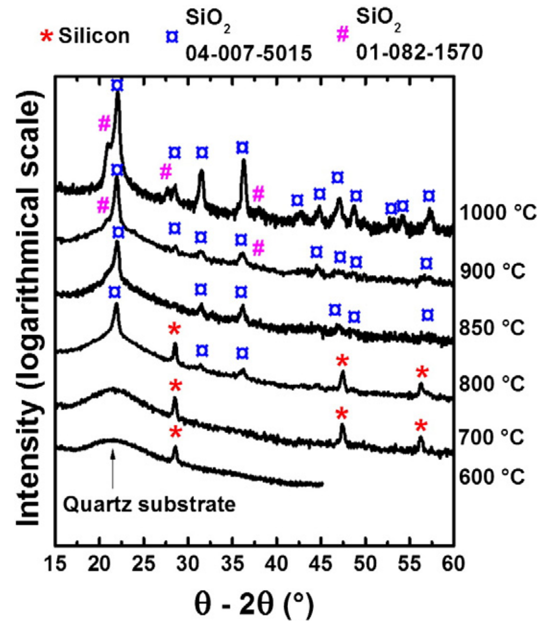

Fig. 8. GI–XRD diffractograms of RTA annealed samples.

As can be observed in Fig. 7, compressive stress, thus oxidation, is much smaller for samples annealed under forming gas (N_2H_2 — 5%). It may be due to a change of major sintering mechanism with the introduction of H_2, which would promote densification and not grain coarsening.

Measured compressive stress lowers when higher Raman laser wavelength is used i.e. with higher probing depth. It may indicate that oxidation of the silicon is stronger at the surface of the sample (Fig. 7). Thermal conductivities of the different thin films have been estimated through the Raman shift method (Fig. 9) [6,18].

Evolution of thermal conductivity is clearly dependent of the annealing atmosphere. Using an inert atmosphere (N_2) thermal conductivity increases very fast. It is an evidence of sintering of Si nanoparticles and reduction of the amount of grain boundaries by grain coarsening. In comparison, annealing under reducing atmosphere (N_2–H_2 5%) is slower. This can be provoked by reduced grain coarsening due to

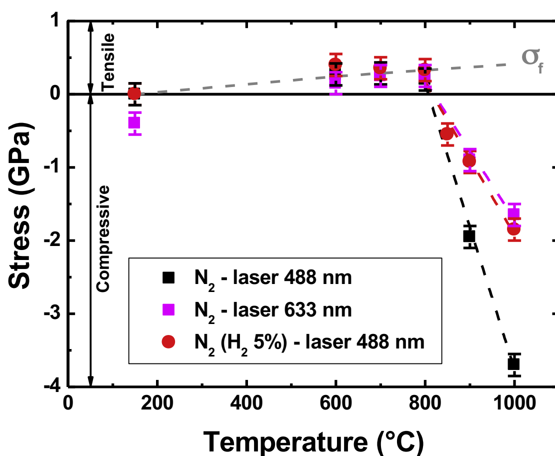

Fig. 7. Evaluation of stress (σ) in the annealed layers (N_2 and N_2–H_2 5%) for two lasers with different probing depth.

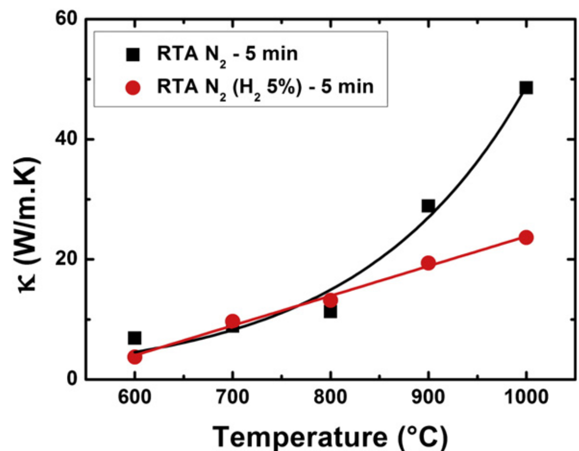

Fig. 9. Thermal conductivity estimation from Raman shift measurement for Rapid Thermal Annealed layer under N_2 and N_2 (H_2 5%) atmospheres. The lines are guides to the eye.

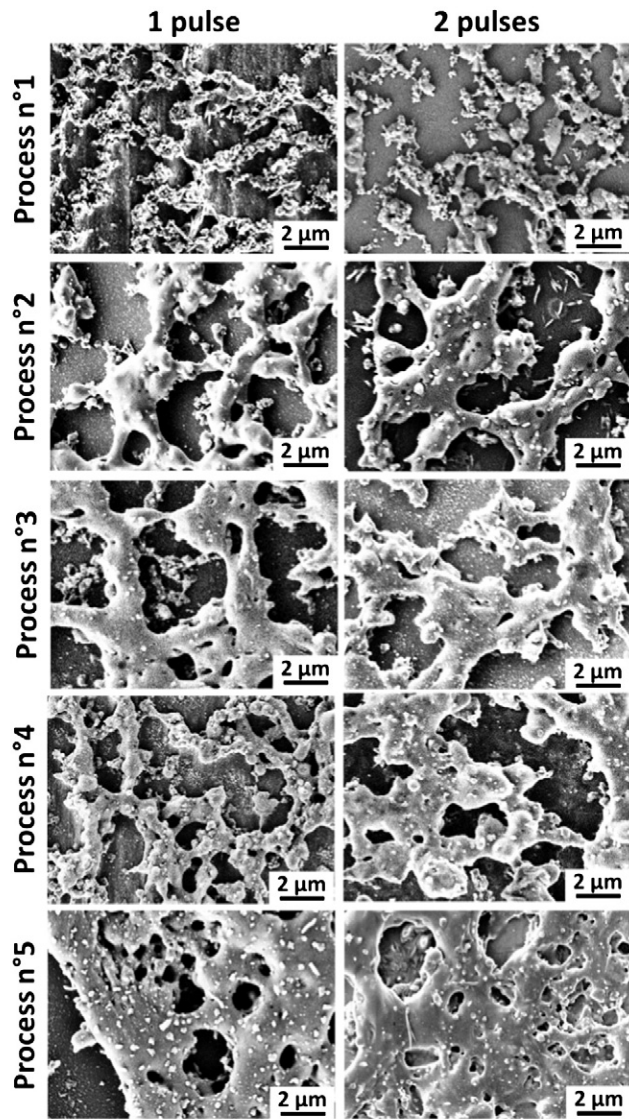

Fig. 10. SEM pictures of photonic sintered inkjet-printed Si NP thin films.

different sintering mechanisms that should promote densification but not grain coarsening [12].

3.3. Photonic annealing of inkjet-printed Si nanoparticles thin films

Photonic annealing is designed for printed electronics. Indeed, the very fast pulse of xenon lamp allows the use of roll-to-roll process and is compatible with flexible and low cost substrates thanks to its selectivity. It is usually used for sintering of metallic (silver and copper) nanoparticles on plastic substrates or paper [35,36].

Concerning Si, this method has been applied in order to crystallize amorphous silicon thin films [37,38] but surprisingly has never been used to sinter silicon nanoparticle thin films. Indeed, the very fast processing is advantageous because it reduces or avoids the oxidation process. Furthermore, the very small thermal conductivity of Si NPs and high absorption coefficient make it a perfect material to use this process since most of the Xe spectrum will be absorbed.

SEM observations after annealing (Fig. 10) show that the thin films are not continuous. Process no. 5, higher energy, gives the layer with the best continuity and NP Si seems to have been melted completely, at least at the top of the layer. At the opposite process no. 1 characterized by the highest value of dissipated power, shows NP Si in necklace with a very low filling area. This process being the most powerful, the Si nanoparticles may have been blown off by the pulse.

Contrarily to SEM pictures that do not show a microstructure difference between same processes repeated 1, 2 or 5 times, thermal conductivity measurements denote a change of microstructure (Table 2).

Furthermore, in Raman measurements performed at low laser power, the peak position of the Si peak does not shift significantly (± 0.3 cm^{-1}, equipment resolution) from c-Si reference position (520.7 cm^{-1}). This is the evidence of reduced oxidation and stress compared to RTA.

Thermal conductivity measurements indicate a change in the microstructure between 2 and 5 repetitions of the pulses. It seems that a threshold of applied power and/or energy must be reached to modify the microstructure after the first pulse process. A special case has to be highlighted, process no. 1 (with the highest power and less energetic) shows amorphization of the thin film after 5 repetitions of the sintering process, while it was the only one to exhibit significant variation of Raman response after 2 repetitions.

In order to better understand those results, simulation of the sintering processes was performed using the software supplied and developed by Novacentrix. SimPulse thermal simulation software allows modeling of the stack of materials (here the Si NP thin film on a silica glass substrate, see Fig. 11-a) and to give an estimation of the temperature for the interfaces between each material [39]. Both most powerful (process no. 1) and most energetic processes (process no. 5) (defined in Table 1) were simulated. Table 3 synthesizes the parameters that have been used for simulations.

Concerning Silica glass substrate, data marked with an asterisk (*) were provided by the supplier (ACM), the others were input in the simulation program. Concerning silicon nanoparticles, some parameters were taken from literature:

- Emissivity: average value of 0.65 has been chosen [40]. It corresponds to the value in the region were Xenon emission is the strongest.
- Absorption coefficient: 10,000 cm^{-1} has been chosen from the literature [8] for a thin film made of crystalline silicon nanoparticles (of equivalent size) deposited by solution process. It corresponds to the absorption coefficient where the xenon lamp emission is the most intense.
- Specific heat: 650 J/kg·K, which is the bulk value. Nevertheless, this value could be underestimated since its value tends to increase with size reduction [41].
- Molecular weight: 28 g/mol is the bulk value.
- Heat of fusion: 50.2 kJ/mol is the bulk value (used for calculation of reduced melting temperature of Si nanocrystals in [28]).
- Heat of vaporization: 359 kJ/mol is the bulk value.

Table 2
Thermal conductivity measurement by Raman spectroscopy of photonic annealed thin films.

Process no.	1	2	3	4	5
κ (W/m·K)					
• 1 process	0.3	0.7	0.8	0.6	0.5
• 2 processes	3.0	0.6	0.8	0.7	1.0
• 5 processes	1.6	3.1	3.4	3.6	4.4

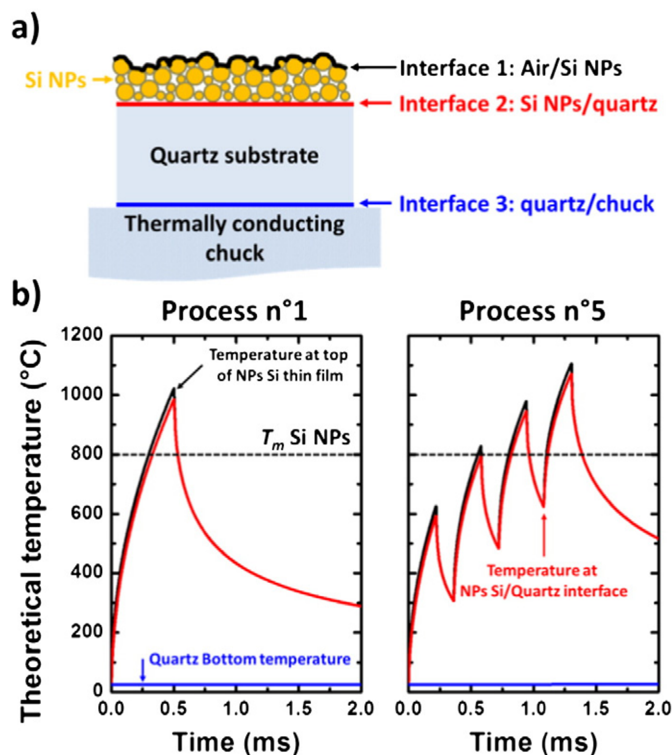

Fig. 11. a) schematic cross section of the stack of materials with identification of the interfaces. b) Thermal simulation of processes no. 1 and no. 5.

The other parameters have been estimated from experiment:

- Melting temperature: 800 °C was estimated from DSC/TGA experiments (Fig. 5).
- Material density: 1.165 g·cm^{-3}, which is half the bulk (2.33 g·cm^{-3} [28]), since the porosity of the thin film is estimated to be at least 50% after inkjet-printing and drying.
- Thermal conductivity of 1 W/m·K (bulk: 144 W/m·K) has been estimated from micro-Raman measurements.
- Thickness: 1 μm was estimated from mechanical profilometry measurements after drying.

Fig. 11-b plots have been obtained using SimPulse program simulating the stack of materials defined in Table 3. They show the temperature at the different interfaces: 1) at the top of the Si NP layer, 2) at the junction between the Si NPs and the silica glass substrate as well as 3) the temperature at the bottom of the silica glass substrate.

The temperature at the top of the Si NP layer is higher than that at the interface with the quartz. Temperature at the bottom of the silica glass substrate is at room temperature (heat sink). As explained before, process no. 1 seems too powerful and to blow off the NP Si layer. Progressive increase of the temperature like that proposed in process no. 5 should be preferred. For both cases the maximum temperature is above the melting temperature measured by DSC/TGA (Fig. 5) and thus explains the continuous morphology of the layers.

Table 3
Parameters input in SimPulse simulation software.

	Si NP thin film	Silica glass substrate
Thickness	1 μm	1 mm*
Melting temperature	800 °C (bulk: 1414 °C)	1683 °C*
Thermal conductivity	1 W/m·K (bulk: 144 W/m·K)	1.4 W/m·K*
Mass density	1.165 g/cm^3 (50% of bulk: 2.33)	2.65 g/cm^3*
Specific heat	650 J/kg·K (same as bulk)	670 J/kg·K*
Emissivity	0.65 (same as bulk)	0.93
Absorption coefficient	10,000 cm^{-1}	0.5 cm^{-1}*
Molecular weight	28 g/mol	60.1 g/mol
Heat of fusion	50.2 kJ/mol	500 kJ/mol
Heat of vaporization	359 kJ/mol	300 kJ/mol

SEM observations and simulations tend to confirm that melting of the tiniest nanoparticles (~20 nm of diameter) occurs during photonic annealing. Almost no peak shift was observed during micro-Raman measurements (at a low laser power) on dried and sintered Si NP thin films. Furthermore, the change in thermal conductivity is very small (some units of W/m·K). It tends to confirm that no grain coarsening occurs during applied processes. This sintering process is therefore a good candidate for applications where the grains must remain at the nanosize level e.g. to increase optical absorption (photovoltaics or photodetectors) or to keep thermal conductivity low (thermoelectric devices).

4. Conclusions

Deposition of inorganic semiconducting materials such as silicon by inkjet-printing is an ambitious objective that would allow the fabrication of devices with high efficiency at low cost. These devices aim mainly at large area energy applications (photovoltaics, thermoelectricity) and display (thin film transistors) applications but could also be used more broadly in electronics. Inkjet-printing of silicon nanoparticles is especially interesting thanks to the modified properties proposed by reducing silicon scale from bulk to the nanosize.

This study focused on the tailoring of the microstructure and thermal conductivity of inkjet-printed silicon nanoparticle thin films for electronic applications such as photovoltaics, thermoelectricity or thin film transistors. Two points were studied: the impact of the nanoparticle surface chemistry on sintering as well as the impact on sintering of the annealing method and atmosphere.

The nanoparticle surface chemistry can be controlled during the ink fabrication. Especially, removal of the silicon dioxide shell was shown to be essential in order to reduce the sintering temperature of the silicon nanoparticles. In this objective, nanoparticles with the addition of NaPMA during the synthesis step were purchased and exhibited reduced melting temperature.

Using these nanoparticles, different annealing processes were studied and compared with the target of reducing the sintering temperature to allow the use of flexible and low cost substrates. Rapid Thermal Annealing allows tailoring of the microstructure from porous layers composed of nanoparticles with limited sintering to a denser layer. Thermal conductivity can therefore be controlled from some units of W/m·K to the half bulk value. Furthermore, grain size and oxidation of the layer can be reduced using a reducing atmosphere.

Finally photonic annealing was used as an innovative sintering method. The process is still not completely controlled but this study confirms that it can be used to fabricate thin films with limited thermal conductivity and limited oxidation. In a near future, this annealing method should allow the fabrication of Si thin films on flexible substrates such as plastic foils (with polyimide as a first step).

Acknowledgments

This work was financially supported by the French National Research Agency (ANR) through the INXILICIUM project. The authors are particularly thankful to J. Loubens (TA Instruments) for the DSC/TGA measurements, Dr. V. Akhavan (Novacentrix) for his great help with the photonic annealing process as well as M. Bimblich and H. Bruyas (ENSM-SE) for the GI–XRD measurements. Helpful discussions with Dr. M. Saadaoui (ENSM-SE/CMP) and J. Mazuir (ENSM-SE) have been particularly appreciated and useful for stress measurement analysis. The silicon nanoparticles were procured from Meliorum Technologies Inc. (620 Park Avenue #145, Rochester, NY14607, USA. Tel.: +1 585 313 0616, fax: +1 585 486 1154, website: www.meliorum.com).

References

[1] OE-A, Organic and Printed Electronics, 2009.
[2] R. Cauchois, M. Saadaoui, A. Yakoub, K. Inal, B. Dubois-Bonvalot, J.-C. Fidalgo, Impact of variable frequency microwave and rapid thermal sintering on microstructure of inkjet-printed silver nanoparticles, J. Mater. Sci. 47 (2012) 7110–7116.
[3] A. Yakoub, M. Saadaoui, P. Benaben, P. Iliev, High efficiency of low-cost spiral antennas for RFID, fully printed by an inline inkjet process, Large Org. Print. Electron. Conf. Proc, LOPE-C 2012, Munich, Allemagne, 2012.
[4] S. Sanaur, A. Whalley, B. Alameddine, M. Carnes, C. Nuckolls, Jet-printed electrodes and semiconducting oligomers for elaboration of organic thin-film transistors, Org. Electron. 7 (2006) 423–427.
[5] Y. Sun, J.A. Rogers, Inorganic semiconductors for flexible electronics, Adv. Mater. 19 (2007) 1897–1916.
[6] E. Drahi, A. Gupta, S. Blayac, S. Saunier, P. Benaben, Characterization of sintered inkjet-printed silicon nanoparticle thin films for thermoelectric devices, Phys. Status Solidi A 211 (2014) 1301–1307.
[7] M. Härting, J. Zhang, D.R. Gamota, D.T. Britton, Fully printed silicon field effect transistors, Appl. Phys. Lett. 94 (2009) 193509.
[8] R.W. Lechner, Silicon Nanocrystal Films for Electronic Applications(PhD Thesis) TU München, 2009.
[9] T. Shimoda, Y. Matsuki, M. Furusawa, T. Aoki, I. Yudasaka, H. Tanaka, H. Iwasawa, D. Wang, M. Miyasaka, Y. Takeuchi, Yasumasa, Solution-processed silicon films and transistors, Nature 440 (2006) 783–786.
[10] E. Drahi, S. Blayac, P. Benaben, Silicon thin-films from nanoparticles dispersion: tailoring morphological, electrical and optical characteristics, MRS Conf. Proc. 1321 (2011).
[11] S. Kirkpatrick, Percolation and conduction, Rev. Mod. Phys. 45 (1973) 574–588.
[12] R.M. German, Sintering Theory and Practice, Wiley-Interscience, 1996.
[13] A.R. Stegner, R.N. Pereira, K. Klein, R.W. Lechner, R. Dietmueller, M.S. Brandt, M. Stutzmann, H. Wiggers, Electronic transport in phosphorus-doped silicon nanocrystal networks, Phys. Rev. Lett. 100 (2008) 18–21.
[14] R.W. Lechner, A.R. Stegner, R.N. Pereira, R. Dietmueller, M.S. Brandt, A. Ebbers, M. Trocha, H. Wiggers, M. Stutzmann, Electronic properties of doped silicon nanocrystal films, J. Appl. Phys. 104 (2008) 053701.
[15] G. Cappelletti, S. Ardizzone, D. Meroni, G. Soliveri, M. Ceotto, C. Biaggi, M. Benaglia, L. Raimondi, Wettability of bare and fluorinated silanes: a combined approach based on surface free energy evaluations and dipole moment calculations, J. Colloid Interface Sci. 389 (2013) 284–291.
[16] R.D. Deegan, O. Bakajin, T.F. Dupont, G. Huber, S.R. Nagel, T.A. Witten, Capillary spreading of liquid drops on solid surfaces, Nature 389 (1997) 827–829.
[17] B.C. Riggs, R. Elupula, V.S. Puli, S.M. Grayson, D.B. Chrisey, Dielectric properties of UV cured thick film polymer networks through high power xenon flash lamp curing, MRS Proc. 1630 (2014).
[18] I. De Wolf, J. Jiménez, J.-P. Landesman, C. Frigeri, P. Braun, E. Da Silva, E. Calvet, Raman and luminescence spectroscopy for microelectronics, Cat. Opt. Phys. Parameters'Nostradamus'Proj. SMT4-CT-95-2024. (1998).
[19] Society-for-Automotive-Engineering, Residual stress measurement by X-ray diffraction, Society-for-Automotive-Engineering, 1971.
[20] M. Nonnenmacher, H.K. Wickramasinghe, Scanning probe microscopy of thermal conductivity and subsurface properties, Appl. Phys. Lett. 61 (1992) 168–170.
[21] F. Hua, M. Qian, Synthesis of self-crosslinking sodium polyacrylate hydrogel and water-absorbing mechanism, J. Mater. Sci. 36 (2001) 731–738.
[22] P.R. Couchman, W.A. Jesser, Thermodynamic theory of size dependence of melting temperature in metals, Nature 269 (1977) 481–483.
[23] G. Guisbiers, L. Buchaillot, Universal size/shape-dependent law for characteristic temperatures, Phys. Lett. A 374 (2009) 305–308.
[24] P. Buffat, J.-P. Borel, Size effect on the melting temperature of gold particles, Phys. Rev. A 13 (1976) 2287–2298.
[25] M. Wautelet, Estimation of the variation of the melting temperature with the size of small particles, on the basis of a surface-phonon instability model, J. Phys. D. Appl. Phys. 24 (1991) 343–346.
[26] A.N.N. Goldstein, The melting of silicon nanocrystals: submicron thin-film structures derived from nanocrystal precursors, Appl. Phys. A Mater. Sci. Process. 62 (1996) 33–37.
[27] S. Bet, A. Kar, Thin film deposition on plastic substrates using silicon nanoparticles and laser nanoforming, Mater. Sci. Eng. B 130 (2006) 228–236.
[28] G. Schierning, R. Theissmann, H. Wiggers, D. Sudfeld, A. Ebbers, D. Franke, V.T. Witusiewicz, M. Apel, Microcrystalline silicon formation by silicon nanoparticles, J. Appl. Phys. 103 (2008) 084305.
[29] C. Greskovich, The effect of small amounts of B and Sn on the sintering of silicon, J. Mater. Sci. 16 (1981) 613–619.
[30] D.R. Stull, H. Prophet, U. States, JANAF thermochemical tables [electronic resource], in: D.R. Stull, H. Prophet (Eds.), Project Directors, 2nd ed, U.S. Dept. of Commerce, National Bureau of Standards, Washington, D.C.1971
[31] J.R. Greer, R.A. Street, Mechanical characterization of solution-derived nanoparticle silver ink thin films, J. Appl. Phys. 101 (2007) 103529.
[32] R. Cauchois, Microstructuration des dépôts imprimés par jet d'encre: de la coalescence des nanoparticules d'argent vers la réalisation d'interconnexions de composants électroniques, Ecole Nationale Supérieure des Mines de Saint Etienne, 2012. (PhD Thesis).
[33] M. Kawata, S. Nadahara, J. Shiozawa, M. Watanabe, T. Katoda, Characterization of stress in doped and undoped polycrystalline silicon before and after annealing or oxidation with laser Raman spectroscopy, J. Electron. Mater. 19 (1990) 407–411.
[34] M. Kawata, T. Katoda, Characterization of stress generated in polycrystalline silicon during thermal oxidation by laser Raman spectroscopy, J. Appl. Phys. 75 (1994) 7456–7459.
[35] K.A. Schroder, S.C. McCool, W.F. Furlan, K. Lane, T.X.P. Suite, Broadcast Photonic Curing of Metallic Nanoparticle Films, in: NSTI Nanotech, MA, Boston, 2006.
[36] J.S. Kang, J. Ryu, H.S. Kim, H.T. Hahn, Sintering of inkjet-printed silver nanoparticles at room temperature using intense pulsed light, J. Electron. Mater. 40 (2011) 2268–2277.
[37] K. Omori, G.S. Ganot, U.J. Chung, A.M. Chitu, A.B. Limanov, J.S. Im, Flash-lamp-induced Lateral Solidification of Thin Si Films, MRS Online Proc. Libr. 1321 (2011).
[38] J.S. Im, Flash Lamp Annealing Crystallization for Large Area Thin Films, WO/2009/111340, 2009.
[39] M.J. Guillot, K.A. Schroder, S.C. McCool, Simulating the thermal response of thin films during photonic curing, in: ASME (Ed.)Proc. 12th Int. Conf. Nucl. Eng. IMECE12, Houston, Texas, USA, 2012, pp. 1–9.
[40] N.M. Ravindra, B. Sopori, O.H. Gokce, S.X. Cheng, A. Shenoy, L. Jin, S. Abedrabbo, W. Chen, Y. Zhang, Emissivity measurements and modeling of silicon-related materials: an overview 1, Int. J. Thermophys. 22 (2001) 1593–1611.
[41] A. Paul, G. Klimeck, M. Luisier, Atomistic modeling of the phonon dispersion and lattice properties of free-standing (100) Si nanowires, 2010 14th Int, Work. Comput. Electron. (2010) 1–4.